

Lawrence Berkeley National Laboratory

Recent Work

Title

Investigation of damage mechanisms in CNT nanocomposites using multiscale analysis

Permalink

<https://escholarship.org/uc/item/7rn6n1rv>

Journal

International Journal of Solids and Structures, 120

ISSN

0020-7683

Authors

Rai, A
Subramanian, N
Chattopadhyay, A

Publication Date

2017-08-01

DOI

10.1016/j.ijsolstr.2017.04.034

License

[CC BY-NC-SA 4.0](#)

Peer reviewed



Investigation of damage mechanisms in CNT nanocomposites using multiscale analysis



Ashwin Rai^a, Nithya Subramanian^a, Aditi Chattopadhyay^{b,*}

^a Graduate Research Associate, School for Engineering of Matter, Transport, and Energy, Arizona State University, Tempe, AZ, 85287, United States

^b Regents' Professor & Ira. A. Fulton Professor of Engineering, School for Engineering of Matter, Transport, and Energy, Arizona State University, Tempe, AZ, 85287, United States

ARTICLE INFO

Article history:

Received 14 September 2016

Revised 20 March 2017

Available online 26 April 2017

Keywords:

Nanocomposites

Carbon nanotubes

Nanomechanics

Multiscale modeling

ABSTRACT

This paper examines microscale and sub-microscale damage mechanisms in carbon nanotube (CNT) reinforced nanocomposites. A multiscale modeling framework with a damage model developed from molecular dynamics simulation, is employed to study the physical mechanisms of damage initiation and propagation in CNT nanocomposites at the sub-microscale. Two CNT arrangements, randomly dispersed and entangled agglomerates, are examined. This investigation offers insights into damage properties of particular configurations of CNTs in a polymer matrix, in addition to specific understanding related to damage concentration effects around the filler material at the sub-microscale. High spatial CNT concentration differential is observed to affect damage initiation and rate of damage. It is further shown to result in sub-microscale crack initiation at low global strains, a phenomenon that is also observed at agglomeration boundaries, which results in CNT agglomerations to behave as crack initiation sites.

© 2017 Elsevier Ltd. All rights reserved.

1. Introduction

The use of carbon nanotubes (CNTs) for structural and multifunctional nanotechnology applications is an area of growing scientific interest (Thostenson et al., 2001; Yu and Kwon, 2009). In particular, nanocomposites that use CNTs as reinforcing nanofillers in the polymer matrix have been shown to exhibit superior multifunctional properties under controlled environments (Balazs et al., 2006), such as improved stiffness (Dean et al., 2006), *in-situ* damage sensing (Datta et al., 2015), precise thermal management (Biercuk et al., 2002) and increased toughness (Coleman et al., 2006), thus presenting potential for unique applications. However, a critical obstacle preventing the integration of nanostructures into practical applications is the inability to scale the performance gains and multifunctional capabilities of nanocomposites for commercialization purposes (Sochi, 2012). In other words, a deep divide remains between the theoretical predictions and the experimental observations of the mechanical, strength, and damage properties of CNT-nanocomposites at the macroscale. These differences translate into limitations, e.g., minimal increase in fracture characteristics (Gojny et al., 2004; Qiu et al., 2007) and low strength and fatigue life compared to predicted values (Ren et al., 2004). Such discrepancies have been attributed to geometrical inconsis-

tencies in the CNT composition at the sub-microscale, such as lack of alignment, agglomerations and poor dispersion of the CNTs (Wicks et al., 2010) that are not accounted for in most macroscale theoretical formulations. Limited efforts have been devoted to a comprehensive analysis of the cause of these discrepancies. Recent studies have shown that the local nanoscale and sub-microscale stress-strain response of nanocomposites can significantly differ from the average bulk response, with the local stress-strain response around the filler material indicating stress concentration sites (Subramanian et al., 2015). Such sub-microscale responses may lead to accelerated damage initiation and may account for the difference in theoretical and predicted macroscale response in these materials.

A number of computational methods have been used to understand the load transfer, elastic behavior, and damage mechanisms of nanocomposites at the nano and sub-microscales (Rai et al., 2016a; Subramanian et al., 2015; Seidel and Lagoudas, 2006; Valavala and Odegard, 2005; Fish and Wagiman, 1993). Molecular dynamics (MD) simulations demonstrate excellent compatibility for resolving the physics associated with load transfer between polymer chains and CNTs, which is possible due to the similarity in length scales between these components (Rahmat and Hubert, 2011). However, MD simulations require high computational times and hence are limited to unit cells of a few nanometers in size. Multiscale modeling methods, on the other hand, may be used for scaling the nanocomposite behavior along multiple length scales,

* Corresponding author.

E-mail address: aditi@asu.edu (A. Chattopadhyay).

since the prevailing mechanisms at the lowest length scale are resolved while maintaining stable solutions at the higher length scales through physical length scale bridging (Subramanian et al., 2015). Multiscale analysis using atomistic simulations is yet another method that is able to not only achieve the desired resolutions for obtaining realistic insights into load transfer and damage mechanisms at the sub-microscale in CNT nanocomposites, but also deliver simultaneously, an accurate far field response. Such a hybrid multiscale approach has been used for investigating the linear and elastoplastic response of CNT nanocomposites (Zhang et al., 2015; Yang et al., 2013; Yang and Cho, 2008), and can also calculate the most likely crosslinking degree of the epoxy after cure (Subramanian et al., 2015) as well as variations in mechanical response due to physical factors, such as CNT orientation, agglomeration, and CNT and polymer interface properties (Alian et al., 2015; Namilae and Chandra, 2005). The multiscale approach has shown to be applicable to a nanocomposite system while simultaneously being reasonably accurate at multiple length scales.

In their recent work, the authors have developed an atomistically informed continuum damage mechanics (CDM) based formulation that captures polymer damage under isothermal conditions and within operating temperatures lower than the glass transition temperature (Rai et al., 2016b). The methodology utilizes bond disassociation energy densities that are calculated from MD simulations of bond breakage in the epoxy polymer chains under load. The bond disassociation energy density is used to formulate the damage evolution curve for a CDM theory which also makes use of polymer mechanics to simulate polymer hardening/softening (Bouvard et al., 2010). This paper extends our previous work by applying the atomistically informed damage model to a CNT/polymer system to achieve a more sophisticated understanding of the load transfer, damage initiation, and propagation in CNT nanocomposites at the length scale of the filler material and its effects at the microscale. This work provides new insights into damage trends, crack initiation, and propagation at the sub-microscale of CNT nanocomposites, and can potentially assist in future nanoengineering of CNT material systems for optimal mechanical response for specific applications.

2. Formulations

This section briefly reviews the multiscale damage formulations developed by the authors (Rai et al., 2016a; 2016b). The developed model has been bench-marked against classical plasticity, and CDM models and verified for experiments involving pure polymer specimens in the following reference: (Rai et al., 2016b). The CDM framework is used to introduce damage at the continuum scale Lemaitre (2012); Chaboche et al. (2006), chosen due to the improved computational efficiency compared to fracture mechanics methods, and for its ability to develop thermodynamically consistent formulations (Coleman and Gurtin, 1967; Simo and Hughes, 2006). The elastic strain, $\underline{\underline{\epsilon}}^e$, the isotropic damage variable, D , the internal variable associated with polymer chain movement and entanglement, ξ , and the original density of the material, ρ_0 , are used to define the Helmholtz specific free energy as:

$$\psi = \frac{1}{\rho_0} \bar{\psi}(\underline{\underline{\epsilon}}^e, D, \xi) \quad (1)$$

The Helmholtz free energy is further used to define the thermodynamic affinities associated with damage, D , and the internal strain due to chain entanglement in the polymer, ξ :

$$Y = -\frac{\partial \bar{\psi}}{\partial D} \quad \text{and} \quad k = \frac{\partial \bar{\psi}}{\partial \xi} \quad (2)$$

The Helmholtz free energy is assumed to be a linear summation of the elastic and inelastic terms. Defining the stiffness matrix as

$\underline{\underline{L}}$, the elastic term of the free energy is obtained using the constitutive relation and the equivalent strain concept (Lemaitre, 2012):

$$\bar{\psi}^e = \frac{1}{2} (1 - D) \underline{\underline{\epsilon}}^e : \underline{\underline{L}} : \underline{\underline{\epsilon}}^e \quad (3)$$

Eq. (3) is used to derive Hooke's law as shown in Eq. (4):

$$\underline{\underline{\sigma}} = \rho \frac{\partial \bar{\psi}}{\partial \underline{\underline{\epsilon}}^e} = (1 - D_\nu)(1 - D) \underline{\underline{L}} : \underline{\underline{\epsilon}}^e \quad (4)$$

The difference in density between the damaged and pristine material can be associated with damage due to volume changes using a dependent variable, D_ν , such that $\frac{\rho}{\rho_0} = 1 - D_\nu$ (Chaboche et al., 2006). D_ν is hence used to quantify the effects of void growth and increase in crack density per unit volume in the material.

The plastic potential is formulated such that the effects of damage and volumetric change is represented (Lemaitre, 1985):

$$\phi_p = \frac{\rho_0}{\rho} \frac{\sigma_{eq}^*}{1 - D} - k - \sigma_y \leq 0 \quad (5)$$

where σ_y is the yield stress. The equivalent stress σ_{eq}^* is chosen to be a variable elliptic function of the first and second stress invariants (Green, 1972; Besson and Guillemer-Neel, 2003; Chaboche et al., 2006) such that the effects of hydrostatic stresses may be considered to determine the plastic state of the material.

The evolution of the state variables need to be defined for implementation of the CDM formulations. The plastic strain rate is obtained using the normality condition:

$$\underline{\underline{\dot{\epsilon}}}^p = \dot{\lambda} \frac{\partial \phi}{\partial (\frac{\rho_0}{\rho} \underline{\underline{\sigma}})} = \frac{\dot{\lambda}}{1 - D} \frac{\partial \sigma_{eq}^*}{\partial \underline{\underline{\sigma}}} \quad (6)$$

where the Peric viscoplastic equation (Perić, 1993) is used to calculate the viscoplastic multiplier $\dot{\lambda}$:

$$\dot{\lambda} = \frac{1}{K} \left[\left(\frac{\phi + \sigma_y}{\sigma_y} \right)^{\frac{1}{n}} - 1 \right] \quad (7)$$

where K and n are the viscoplastic constants.

Elements of polymer mechanics are included to simulate the process of chain motion, linkage, and entanglement. The evolution of the internal strain in the polymer is controlled by the increase in internal energy due to entanglement of the polymer chains and the subsequent energy release due to the co-operative movement of the polymer chains at release. When polymer chains become entangled an internal strain like quantity, defined by ξ , is produced. Anand and Gurtin (2003) developed equations to describe the evolution of this quantity, which was further simplified by Bouvard et al. (2010) and is presented in Eqs. (8) and (9):

$$\dot{\xi} = h_0 \left(1 - \frac{\xi}{\xi^*} \right) \dot{\lambda} \quad (8)$$

$$\dot{\xi}^* = g_0 \left(1 - \frac{\xi^*}{\xi_{sat}^*} \right) \dot{\lambda} \quad (9)$$

The internal strains evolution equation simulates the obstacles to chain movements such as entanglement points. ξ^* is the energy barrier opposing chain movement and as further chains escape the entanglement points, this barrier is lowered resulting in further increased motion of chains. Further details on this procedure can be found in Rai et al. (2016b).

The damage evolution equation is formulated from the MD simulation results of the bond disassociation energy density variation under applied strain. A recently developed hybrid MD simulation framework that utilizes reactive force fields was used to characterize the energy variations caused by successive bond breakages at

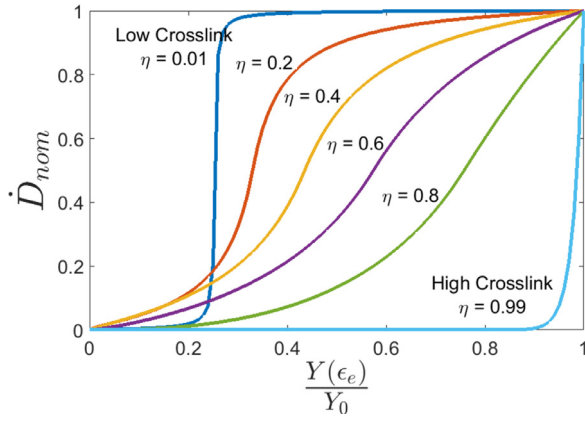


Fig. 1. Damage evolution for different crosslinking degrees.

the nanoscale in thermoset polymers under isothermal conditions and at operating temperatures below the glass transition temperature (Subramanian et al., 2015). It can be noted that molecular sliding and entanglement is an inherent aspect of these non-linear molecular simulations which can also lead to local covalent bond breakages due to local bond stretching. The entanglement is thus intimately coupled with the phenomenon of bond breakage which is captured in the bond energy density variations. The continuum equation for the damage evolution, as shown in Eq. (10), reproduces the atomistic damage process and is developed with parameters that vary according to the crosslinking degree, η .

$$\dot{D} = \frac{\dot{\lambda}}{2} \cdot \left[\text{sgn}(\chi) \cdot \frac{-(1-\eta)|\chi| - |\chi|}{-2(1-\eta)|\chi| + (1-\eta) - 1} + 1 \right] \quad (10)$$

where $\text{sgn}()$ is the signum function and χ is defined as:

$$\chi = 2 \left(\frac{Y}{Y_0} \right)^{\frac{1}{2(1-\eta)}} - 1 \quad (11)$$

where Y is the elastic energy of the system and Y_0 is a material parameter associated with the maximum energy required to initiate damage in the material. Fig. 1 shows the variation of nominal rate of damage $\dot{D}(\dot{\lambda} = 1)$ versus normalized elastic energy $\frac{Y}{Y_0}$. Furthermore, MD simulations of the epoxy/hardener system was shown to be isotropic for a unit cell size of 343 nm^3 (cube with edge length of 7 nm) with around 40,000 atoms (Subramanian et al., 2015; Zhang et al., 2015). In this work the distance between any two consecutive nodes, at the continuum scale, of the polymer system was maintained to be much larger than 7 nm to ensure isotropy of the pure polymer, assuming each continuum nodal point behaves as a homogenized polymer MD unit cell.

3. Experimental validation

Damage model applicability is tested by comparing the predictions from the numerical simulation to the results from an open-hole tension experiment. The specimen was manufactured using epoxy resin, diglycidyl ether of bisphenol F (DGEBF), and hardener diethylenetriamine (DETA). The design and manufacturing of the specimen, as well as experimental procedure is based on ASTM standard D638 (ASTM-D638-14, 2014), as modified by Fard et al. (2011) for the testing of open-hole polymer specimens. Specimen details are presented in Table 1 and Fig. 2.

To begin the testing process, the specimen is gripped at the ends using hydraulic grips in an MTS mechanical testing machine. 3-D Digital Image Correlation (DIC) was used to measure the displacement and strain field contours on the surface of the open-hole test specimen. The DIC system takes digital images during the

Table 1
Open-hole specimen dimensions.

Dimensions	C	D	L	LO	T	W	WO
Values (mm)	3.5	58.5	32.5	97.5	3.5	13	26

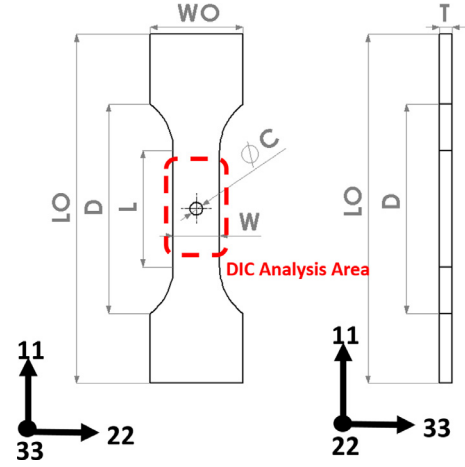
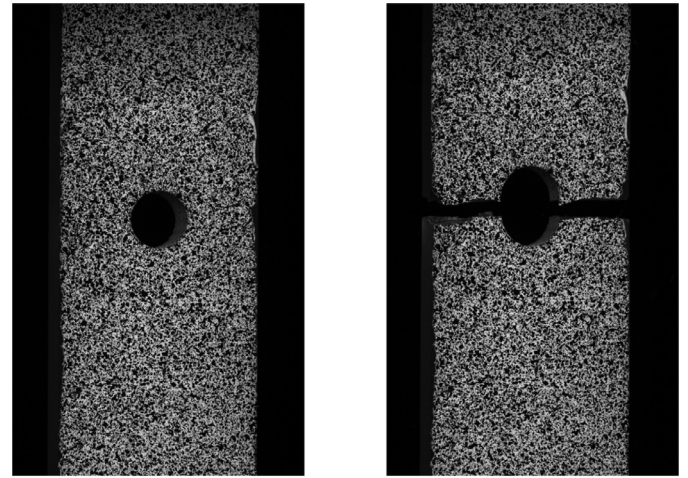


Fig. 2. Open-hole specimen details.



(a) Unloaded configuration

(b) Failed specimen

Fig. 3. Open-hole test specimen displaying speckle pattern.

experiment and then tracks a random speckle pattern shown in Fig. 3, which is painted on the surface of the specimen to calculate relative and rigid body displacements. The displacement field is post-processed to obtain corresponding strain fields. The stereovision capabilities of DIC ensures a highly accurate in-plane and out-of-plane displacement and strain measure of a surface.

The specimen was tested in displacement control at a rate of 1 mm min^{-1} to ensure quasistatic conditions. The displacement and strain field calculations were performed only for the stem portion of the test coupon, as shown in Fig. 2. Rigid body displacement of the specimen from the DIC results was used to calculate and ensure minimal grip slip. A numerical model of the specimen is generated in Abaqus, a commercial FE package, and then virtually tested under the same conditions as the experiment. The formulations presented in Section 2 are implemented in Abaqus using a user sub-routine with damage model parameters detailed in

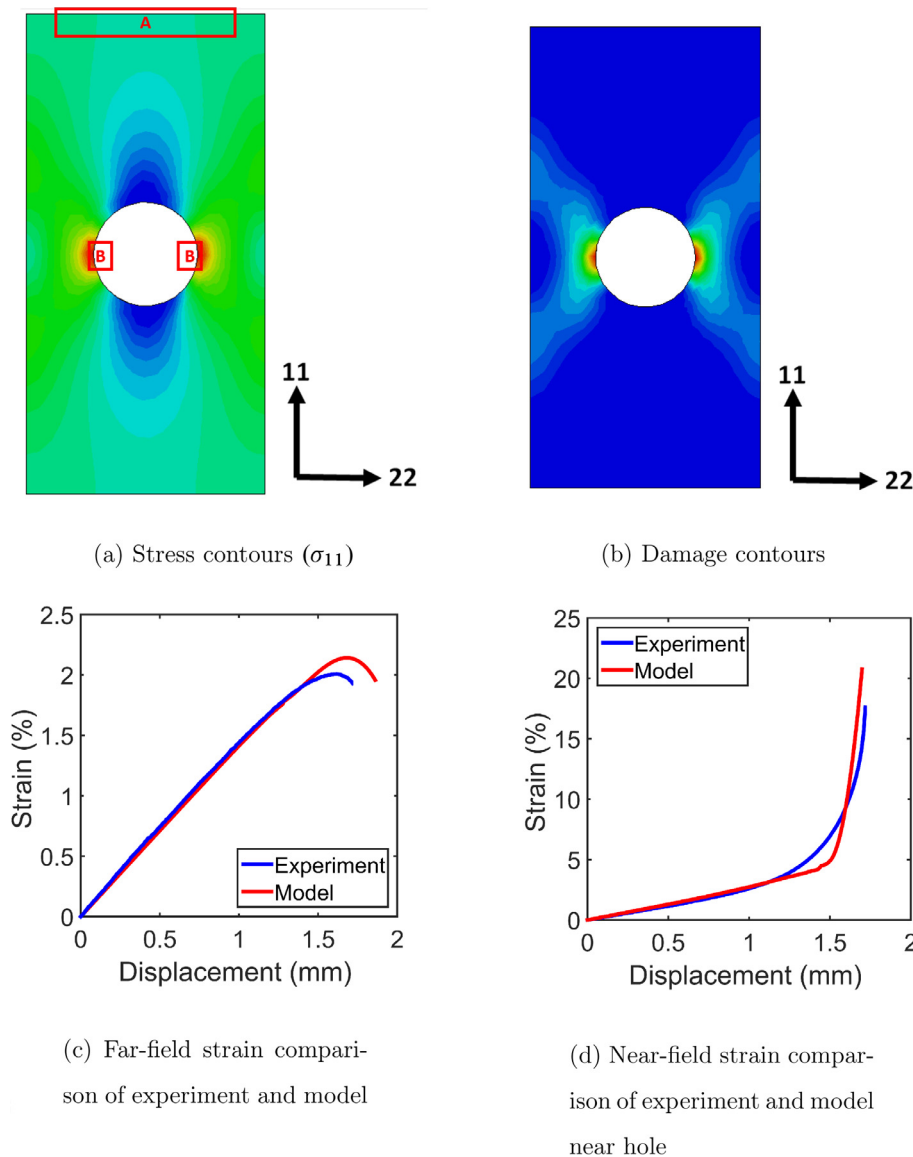


Fig. 4. FE model and test comparison.

Table 2

Damage model parameters obtained from previous investigations (Rai et al., 2016b).

η	0.19	h_0	2
$\dot{\epsilon}$	0.005 s ⁻¹	g_0	1
K	15	ξ_{sat}	0.08
n	2.5	ξ_0	0.12
σ_y	63.375 MPa	C_k	2.8 GPa
Y_0	0.12 MPa		

Table 2 and then applied to the polymer material. The numerical model is meshed with 1550 3-D C3D8R solid brick elements with reduced integration. A finer mesh is generated near the hole to capture the stress concentration effects. Only the stem portion of the experimental specimen is modeled. The boundary conditions emulate the experiment with the bottom surface constrained in 11 direction (orientation can be seen in Fig. 2) and a displacement load applied at the upper surface in the positive 11 direction under quasi-static conditions.

The stress contours in the loading direction (σ_{11}) obtained from the FE simulation are shown in Fig. 4a, where the classical stress concentration contours around the open-hole can be observed. The

damage contours in Fig. 4b show a clear cross localization pattern at the onset of nonlinear behavior around the region. Fig. 4c shows the comparison of the far field strain between the experimental results and the FE model versus the applied displacement. The reported strain is an average of the strain measured at a few points far from the hole and in the loading direction (ϵ_{11}) which is shown as section A in Fig. 4a. To maintain a fair comparison, the strains were measured at the same points in the FE model as the DIC images of the experiment. It can be seen that nonlinearity in far field strains and complete fracture of the specimen were captured reasonably well by the model.

Fig. 4d shows the strain evolution (ϵ_{11}) around the field of the hole. These strains were measured as an average value taken from section B in Fig. 4a. The local area around the hole experiences increased stresses due to the concentration effects and, at larger crosshead displacements, this leads to concentrated plasticity and damage in the polymeric material relative to the far field regions. This phenomenon is exhibited as nonlinearly increasing strains in Fig. 4d. The slight mismatch around 5% strain is attributed to the plasticity algorithm which depends on the plastic potential activating the damage formulations. This mismatch can be corrected by taking better measures of the yield point for the damage formula-

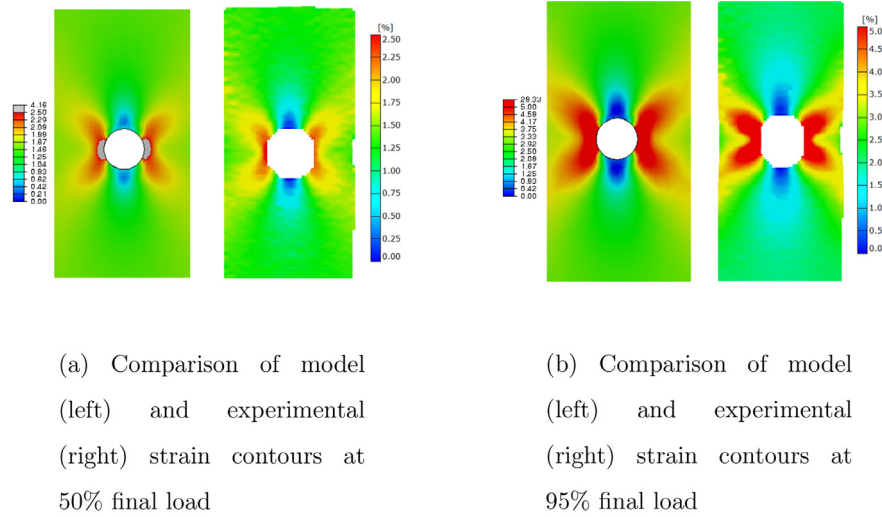


Fig. 5. Strain contour comparison of model and experiment.

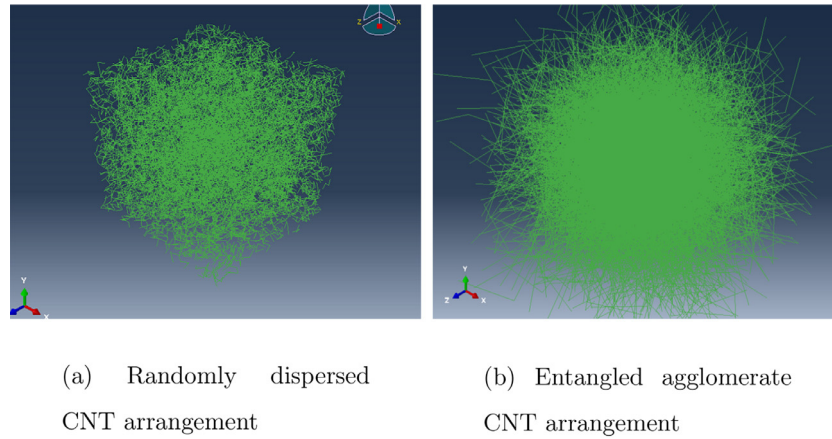


Fig. 6. CNT mesh.

tion and, in future work, will be evaluated based on MD simulations of the polymer. The strain contours in the loading direction (ϵ_{11}) from the experiment, as captured by the DIC software, is then compared against the strain contours from the FE model in Fig. 5a and b. It can be seen that the model closely follows the experimental results in the far field regions and at the local region around the hole, while capturing the nonlinear increase in strains and the resulting fracture due to local plasticity and damage, which are the essential characteristics of the open-hole test.

4. Microscale model

The damage model detailed in Section 2 and validated in Section 3 is incorporated into a microscale model to investigate the microscale and sub-microscale load transfer and damage effects of CNTs in a polymer matrix. A microscale RVE of the polymer is generated in the FE framework and CNTs are inserted into the polymer model by explicitly modeling them using a vertex generation algorithm in the FE global coordinate system. Each vertex of the CNT is assigned a coordinate $(x_i, y_i, z_i)^j$, where i denotes the vertex number and j denotes the CNT. The general procedure of modeling the CNTs was developed by the authors Rai et al. (2016b) and is extended in this paper to study two different arrangements of CNTs: (i) randomly dispersed and (ii) entangled agglomerates, which are shown in Fig. 6. The randomly dispersed CNT arrangement is indicative of a nanocomposite system

wherein the CNTs are thoroughly mixed in the matrix. A realistic composition of CNTs in a randomly dispersed arrangement involves CNTs that may or may not be uniformly spaced apart from each other, but will not form entangled agglomerates. However it may be possible for local bunching of a few CNTs (<10 CNT) to take place. Entangled agglomerates are modeled as dense spheres of CNTs (>100 CNT) as they are generally observed under transmission electron microscopy images (Li et al., 2007). The agglomerated CNT arrangement is generated by constraining the first vertex of the CNT such that it remains inside a sphere with the radius equal to the agglomerate radius, r_{agg} . The agglomerate radius is chosen to be one fourth of the RVE dimensions in this work to include as much of a far field effect as possible while maintaining computational economy. The first vertex of the CNT in the entangled agglomerate arrangement can then be calculated using:

$$\begin{aligned} x_1^j &= r_{agg} \cos(\theta) \sin(\cos^{-1}(\phi)) \\ y_1^j &= r_{agg} \sin(\theta) \sin(\cos^{-1}(\phi)) \\ z_1^j &= r_{agg} \cos(\cos^{-1}(\phi)) \end{aligned} \quad (12)$$

Where $\theta = 2\pi\alpha$, $\phi = 2\alpha - 1$ and α is a randomly generated value between 0 and 1. The remaining vertices of the CNT are calculated using a random vertex generation formula described by Eq. (13). Unlike the agglomeration case, all the vertices in the randomly dis-

Table 3
Table of CNT properties.

CNT length	0.5 μm
CNT Dia	9 nm
Type	Single walled
Elastic modulus	475 GPa
Poisson's ratio (ν)	0.35

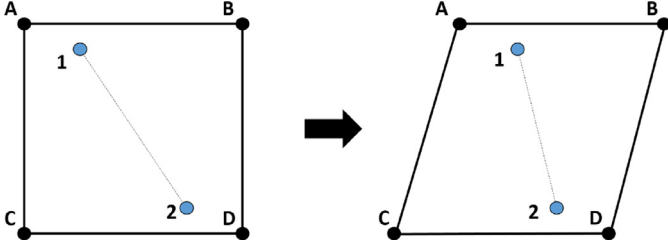


Fig. 7. Schematic of the embedded element technique.

persed arrangement are generated using Eq. (13).

$$\begin{aligned} x_i^j &= L_{\text{CNT}} \sqrt{1 - \phi^2} \cos(\theta) \\ y_i^j &= L_{\text{CNT}} \sqrt{1 - \phi^2} \sin(\theta) \\ z_i^j &= L_{\text{CNT}} \phi \end{aligned} \quad (13)$$

where L_{CNT} is the length of a segment of the CNT generated. The CNT algorithm generates 7 segments with 8 vertices per CNT. Three dimensional truss elements are used to model the CNTs to represent the structural reinforcement provided by the nanofillers. Each nanocomposite model contains 2000 CNTs. The waviness, radius, length and material properties of the CNTs can be controlled to model either fully stochastic CNT systems or ordered ideal CNT arrangements. The material properties and dimensions of the CNTs used in this work are reported in Table 3 (Romanov et al., 2015).

The nanocomposite model, generated using the algorithm described previously, is irregular and difficult to mesh using conventional techniques. Hence, the approach of embedded elements is used to achieve the meshing required in this case (Dolbow and Harari, 2009). The embedded element technique allows the constraining of the nodal translational degrees of freedom of a group of elements that lie embedded in a group of host elements. In this technique, the embedded nodal degrees of freedom are appropriately interpolated from the values of the nodal degrees of freedom of the host elements (Hibbit et al., 2007).

A schematic of the embedded technique is displayed in Fig. 7. In this schematic, the host element is made of nodes A–B–C–D and nodes 1–2 belong to the embedded element. The displacement of node 1 is calculated by appropriate weight factors determined based on the geometric location of node 1 in the host element and hence, is mainly influenced by the displacements of nodes A–B. Similarly, node 2 displacement is mainly influenced by the displacements of nodes C–D. Consequentially, the displacement field of the host element is influenced by the presence of the embedded element and its stiffness properties. The embedded element displacements are therefore obtained without the need for intermediate nodes as would be the case in a conventionally meshed model.

The method of embedded elements for the modeling of CNTs within polymer has been previously demonstrated by Romanov et al. (2013, 2015) and the authors (Rai et al., 2016a, 2016b). The polymer model is generated using 5000 elements of 8-noded 3-D solid C3D8 brick element and used as the host mesh within which, the CNT elements are embedded. The translational degrees of freedom of the embedded elements are constrained to the response of the polymer mesh. This technique provides a computationally

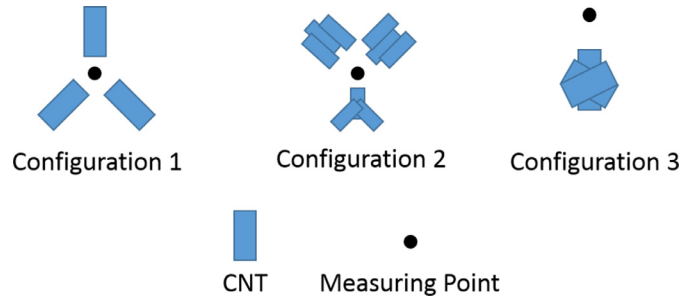


Fig. 8. Schematic of the CNT configurations in the randomly dispersed CNT model.

efficient means of generating a complicated nanocomposite model while minimizing the total degrees of freedom. Furthermore, periodic boundary conditions are applied to the edges of the nanocomposite model to simulate the periodic behavior of the RVE (Rai et al., 2016b).

5. Microscale model results

5.1. CNT configuration effects

The microscale nanocomposite model with randomly dispersed CNTs is generated according to the procedure detailed in Section 4 and is tested in Abaqus with the damage model applied using a user subroutine. It should be noted that the continuum hypothesis for this model with CNTs was verified in a previous work (Rai et al., 2016b). The model is tested in tension and representative results are reported in this section. Unless otherwise mentioned, the measured stress is in the loading direction (σ_{11}). The local stress–strain response is obtained by measuring the local stress (σ_{11}^l) versus the local strain (ϵ_{11}^l). The global stress–strain response is obtained by ensemble averaging the stress (σ_{11}) and strain (ϵ_{11}) values for the whole model as represented in Eq. (14).

$$\sigma_{11} = \frac{1}{V} \int \sigma_{11}^l dV \quad \epsilon_{11} = \frac{1}{V} \int \epsilon_{11}^l dV \quad (14)$$

The arrangement shown in Fig. 6a can be scanned at the sub micro length scale to make certain local patterns of CNTs apparent using virtual voxels. The voxels isolate a sub-volume of the nanocomposite material so that local CNT patterns can be discerned and studied from the larger mass that is shown in Fig. 6a. Each voxel contains around 5–15 CNTs. Due to the random nature of the arrangement in Fig. 6a, some of these voxels are denser than others. This simulates highly dispersed CNTs within an epoxy volume. The pattern of CNTs observed within these sub-volumes can then be reduced to three configurations.

A schematic of the three configurations is shown in Fig. 8. Configuration 1 represents a sub-volume containing approximately uniformly dispersed CNTs, arranged symmetrically within the sub-volume. The CNTs do not bunch together and are approximately equally spaced apart. Configuration 2 represents a sub-volume that contains a relatively large amount of CNTs. These CNTs lie very close to each other forming local bunches. However, the CNTs are nearly symmetric with respect to each other within the sub-volume such that there is an even spatial variation in stiffness. Configuration 3 represents sub-volumes that are surrounded by a single bunch of CNTs asymmetrically present within the cubic sub-volume. This configuration exhibits a relatively large matrix rich area and an uneven spatial variation in stiffness within the sub-volume. It is important to note that the bunched CNTs referenced in this section do not represent agglomeration. In this case a bunch of CNTs contains a small number (<10) while agglomerations contain a relatively larger number of CNTs (>100). Additionally, a few

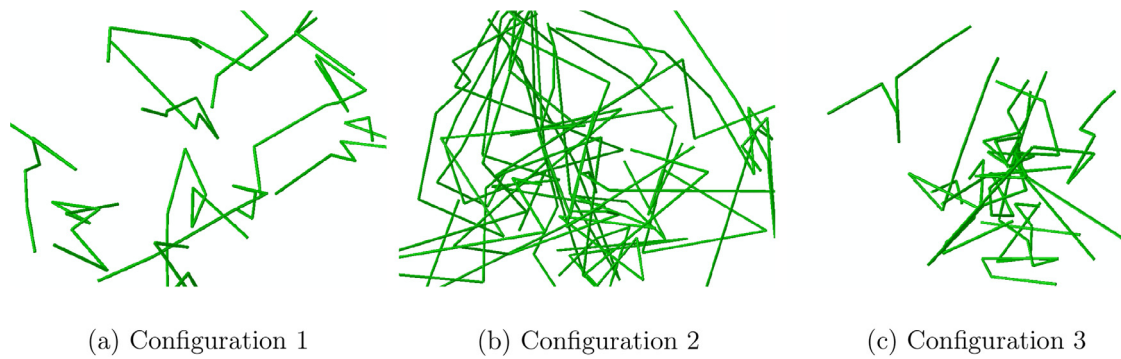


Fig. 9. Representative CNT configurations images from the CNT model.

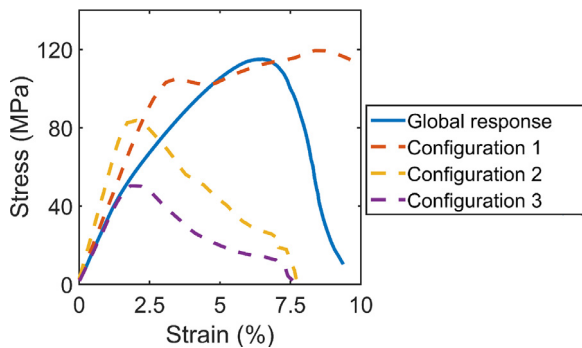


Fig. 10. Stress-strain response for different configurations of CNTs.

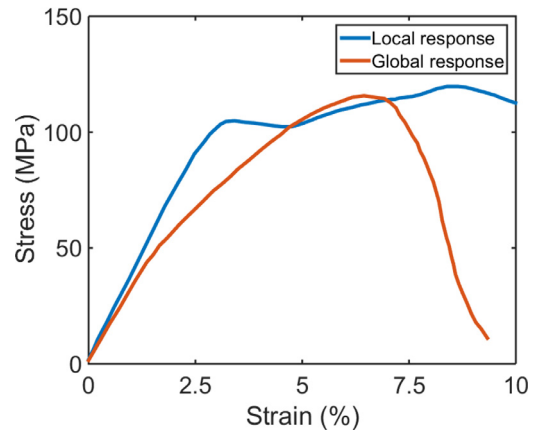


Fig. 11. Global and local stress-strain response (Rai et al., 2016b).

other patterns were observed such as sub-volumes with zero CNTs, however, such sub-volumes were rare and not studied independently. Fig. 9 exhibits representative images for each configuration from the model. The beam rendering option in Abaqus was utilized to show the cylindrical geometry in these images.

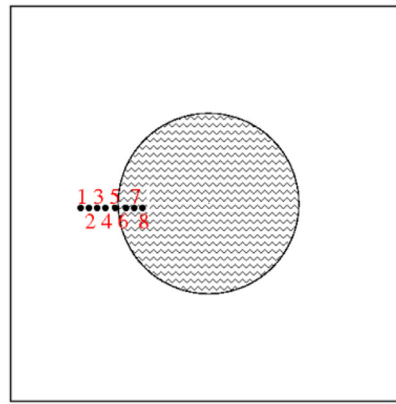
Fig. 10 shows the difference between the global loading direction stress-strain response of the microscale nanocomposite RVE and the local stress-strain response at the sub-microscale around the CNT nanofillers within the nanocomposite. The local response of the sub-volumes is the averaged response for similar configurations surveyed within the larger mass. It was observed that local configurations of the CNTs at the sub-microscale significantly affected the local stress-strain behavior and the damage characteristics. Configuration 1 exhibits the most delayed damage initiation and damage progression relative to the other configurations. The stress-strain response of configuration 1 is similar to the response observed locally near a single CNT in a nanocomposite where the CNTs are ideally structured and spaced apart. The authors have shown in a previous study that the stress-strain response of a single CNT in a polymer network exhibits a unique trend. The mechanical response of a single CNT in a polymer network, obtained through elasto-plastic molecular dynamics simulations, showed an initial peak followed by softening, a recovery phase and secondary softening up to failure (Subramanian et al., 2015). The authors have also shown that a similar response can be registered at the continuum scale in an FE model with atomistically informed multiscale damage formulations for a CNT in polymer matrix, as exhibited in Fig. 11 (Rai et al., 2016b). The unique stress-strain response displayed by configuration 1 is only possible due to the spacing and symmetric structure of this configuration. Furthermore, this also suggests that the MD simulation of a CNT polymer unit cell represents an ideally spaced CNT structure due to the periodic conditions applied at the edges of the MD unit cell.

Configuration 2 shows early damage relative to configuration 1 and also displays faster damage evolution leading to acceler-

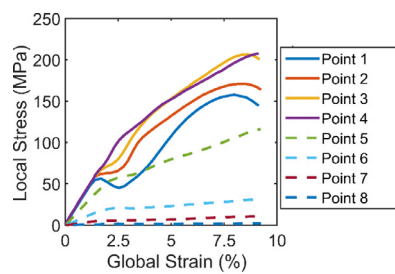
ated local failure. This occurs due to the large stiffness differential between the CNT bunches and the surrounding matrix. However, configuration 2 shows relatively better load transfer compared to configuration 3, due to the proximity of neighboring CNTs and displays better damage characteristics than configuration 3. Configuration 3 shows earliest damage initiation relative to the other configurations and rapid damage evolution due to the large stiffness differential between CNT-rich and CNT-free area. Configuration 3 contains a large matrix rich zone which causes the large spatial stiffness differential and poor load transfer characteristics, since this configuration also lacks neighboring CNTs, leading to rapid damage escalation and local failure. The global microscale response can also be seen in Fig. 10 which is the aggregate response of all the local configurations, including the representative ones presented in this section. It is observed that the global response is significantly different compared to the various local responses due to the complex sub-microscale mechanics and interactions that influence the local response.

5.2. Agglomeration effects

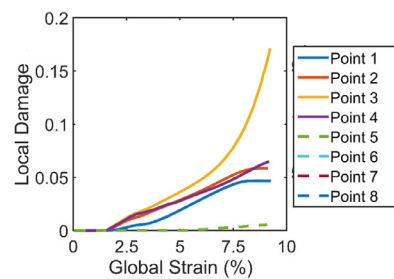
The microscale nanocomposite model with entangled CNT agglomerate arrangement is tested in Abaqus under the same conditions as the randomly dispersed CNT model. The stress variations in the matrix of the agglomerate nanocomposite model is studied. It is observed that the matrix within the agglomerate displays a stress free condition while the matrix surrounding the agglomerate is under high tensile stress. Since, the matrix is present throughout the agglomerate in this model, this would physically represent a state of high degree of wetting leading to high permeability of the polymer within the entangled CNT agglomerate.



(a) Chosen points about the agglomerate



(b) Stress at chosen points



(c) Damage at chosen points

Fig. 12. Stress and damage profile about the agglomerate.

In order to better understand the stress variation and damage progression in the matrix constituent around the agglomerate, a set of 8 points were chosen such that points 1–3 appear at the immediate exterior of the agglomerate, points 4–5 appear at the interphase of the agglomerate and the matrix, and points 6–8 appear in the interior of the agglomerate. The chosen measuring points permits the study of the spatial transition of stress fields in the matrix from the exterior of the interphase to the interior. A schematic of the chosen points relative to the agglomerate is shown in Fig. 12a. Fig. 12b shows the local stress response compared to the globally applied strain at each of the chosen measuring points. The stress is measured in the direction of loading and is local to the measuring point.

A transition in the stress field in the matrix is apparent with the zones exterior to the agglomerate exhibiting the unique stress-strain response discussed previously. The zone exterior to the agglomerate boundary contains loose strands of CNTs. These are the ends of the CNTs entangled within the agglomerate. At the sub-microscale these strands can represent equally spaced CNTs. The interphase zone (the agglomerate boundary) is relatively more CNT-dense than the agglomerate exterior and the stress field transitions in the matrix to a brittle-like nature in this zone. The stress field in the matrix inside the agglomerate is minimal or nonexistent due to the high concentration of CNTs in this region. The CNTs dominate the load transfer mechanism within the agglomerate and produces a stress free condition in the matrix. Fig. 12c displays the damage in the matrix at each of the chosen measuring points and can be used to visualize the transition in damage evolution between the matrix at the agglomerate exterior and the interior. It is observed that maximum damage occurs at the interphase region between the matrix and the agglomerate. This damage profile in-

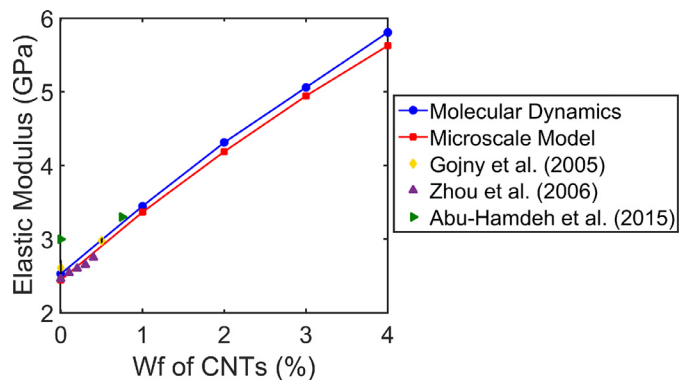


Fig. 13. Variation of elastic modulus with weight fraction of CNTs.

indicates a separation of the polymer and the agglomerate surfaces leading to crack formation, concentrated around the interphase region. These microcracks lead to rapid damage propagation leading to global failure. Experimental work on CNT-epoxy systems have shown similar results, with CNT agglomerates acting as stress concentration and damage initiation sites (Zhou et al., 2008). Thus, entangled agglomerates in close contact could lead to interaction of the microcracks forming at this region and the consequent rapid failure of the overall system.

5.3. Variation with weight fraction of CNTs

Fig. 13 shows the variation of the global material response of the randomly dispersed nanocomposite model with change in

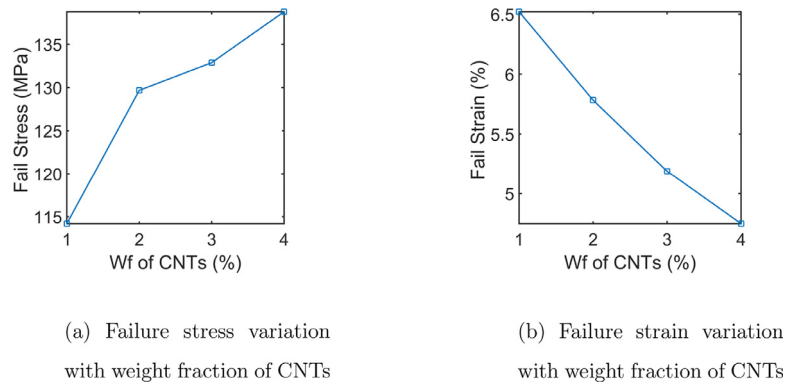


Fig. 14. Failure property variation with weight fraction of CNTs.

weight fraction of CNTs. It was observed that an increase in the weight fraction of CNTs led to increase in the elastic modulus, however the relationship is not strictly linear. The elastic modulus obtained from the microscale model is compared with results obtained from various experimental investigations (Gojny et al., 2005; Zhou et al., 2007; Abu-Hamdeh and Alnefaie, 2015) and from MD simulations (Subramanian et al., 2015). The global failure stresses and strains with respect to change in weight fraction of CNTs is presented in Fig. 14. The increase in weight fraction of CNTs causes increased brittle response with higher failure stress but lower failure strain. An increase in weight fraction of CNTs leads to an increase in the amount of various sub-optimal sub-micro configuration of CNTs. Though the larger number of CNTs leads to higher global elastic properties, the randomness of orientation and larger sub-optimal sub-micro CNT configurations lead to an increase in 'hotspot' areas compared to lower CNT weight fraction material. These hotspot areas combine with larger differentials in internal stresses in the polymer to cause faster damage initiation and propagation in the material leading to lower failure strains for higher weight fraction of CNTs.

6. Conclusion

In this paper a multiscale continuum damage mechanics based formulation was utilized to quantify the damage and consequent stress-state at the micro and sub-microscale in CNT nanocomposites. This formulation was first validated at and then used in a microscale model of nanocomposites with the CNTs modeled in randomly dispersed and entangled agglomerate arrangements. Through these simulations some insight on the sub-microscale damage effects in nanocomposites was gained:

(i) Damage from MD simulations of bond breakage in nanocomposites can be used at the continuum scale using CDM formulations; (ii) the unique nanoscale stress-strain response obtained from CNT-epoxy MD simulations is also observed at the continuum scale, however, it is found to be a highly localized phenomenon occurring in the immediate vicinity of evenly spaced CNTs. This leads to an explanation of the physical representation of the uniaxial stress/strain results obtained from MD at the microscale. It also shows the context of even spacing of CNTs in the MD results; (iii) the most desirable material response is obtained when the CNTs are spaced evenly apart from each other, however this is difficult to achieve in practice. The least desirable response occurs when small bunches of CNTs form asymmetrically in a matrix rich region. This phenomenon emphasizes the need to include local information in the study of CNT nanocomposites. This also highlights the need for effective CNT dispersion during the manufacturing of CNT nanocomposites; (iv) the insights reported in this work can be used to create realistic physics based knock down factors for classi-

cal idealistic formulations to represent damage initiation and progression rather than using empirical factors (v) agglomerates produce a stress free region in the interior and cause a radial separation between the polymer and the agglomerate surfaces due to the large spatial variation in stiffness between the agglomerate and the polymer.

With the development of this multiscale methodology and with the insights provided in this paper, better multiscale models of nanocomposites can be created to accurately predict damage and explain highly complex fracture in nanocomposites. Furthermore, such models may be used to nanoengineer improvements in nanocomposites by modifying the CNT architecture to mitigate damage initiation and propagation.

Acknowledgment

This research is supported by the Office of Naval Research (ONR), Grant number: N00014-14-1-0068. The program manager is Mr. William Nickerson.

References

- Abu-Hamdeh, N., Alnefaie, K., 2015. Mechanical properties and gradient effects of carbon nanotube as polymer nanocomposites. In: International Conference on Computer Information Systems and Industrial Applications. Bangkok, Thailand, pp. 626–628.
- Alian, A., Kundalwal, S., Meguid, S., 2015. Multiscale modeling of carbon nanotube epoxy composites. *Polymer* 70, 149–160.
- Anand, L., Gurtin, M.E., 2003. A theory of amorphous solids undergoing large deformations, with application to polymeric glasses. *Int. J. Solids Struct.* 40 (6), 1465–1487.
- ASTM-D638-14, 2014. Standard Test Method for Tensile Properties of Plastics. West Conshohocken, PA: ASTM International.
- Balazs, A.C., Emrick, T., Russell, T.P., 2006. Nanoparticle polymer composites: where two small worlds meet. *Science* 314 (5802), 1107–1110.
- Besson, J., Guillemer-Neel, C., 2003. An extension of the green and guron models to kinematic hardening. *Mech. Mater.* 35 (1), 1–18.
- Biercuk, M., Llaguno, M.C., Radosavljevic, M., Hyun, J., Johnson, A.T., Fischer, J.E., 2002. Carbon nanotube composites for thermal management. *Appl. Phys. Lett.* 80 (15), 2767–2769.
- Bouvard, J., Ward, D., Hossain, D., Marin, E., Bammann, D., Horstemeyer, M., 2010. A general inelastic internal state variable model for amorphous glassy polymers. *Acta Mech.* 213 (1–2), 71–96.
- Chaboche, J., Boudifa, M., Saanouni, K., 2006. A cdm approach of ductile damage with plastic compressibility. *Int. J. Fract.* 137 (1–4), 51–75.
- Coleman, B.D., Gurtin, M.E., 1967. Thermodynamics with internal state variables. *J. Chem. Phys.* 47 (2), 597–613.
- Coleman, J.N., Khan, U., Blau, W.J., Gun'ko, Y.K., 2006. Small but strong: a review of the mechanical properties of carbon nanotube–polymer composites. *Carbon* 44 (9), 1624–1652.
- Datta, S., Fard, M., Johnston, J., Quigley, E., Chattopadhyay, A., 2015. In-situ strain and damage sensing in glass fiber laminates using embedded cnt. *Struct. Health Monitor.*
- Dean, D., Obore, A.M., Richmond, S., Nyairo, E., 2006. Multiscale fiber-reinforced nanocomposites: synthesis, processing and properties. *Compos. Sci. Technol.* 66 (13), 2135–2142.
- Dolbow, J., Harari, I., 2009. An efficient finite element method for embedded interface problems. *Int. J. Numer. Methods Eng.* 78 (2), 229–252.

- Fard, M.Y., Liu, Y., Chattopadhyay, A., 2011. Characterization of epoxy resin including strain rate effects using digital image correlation system. *J. Aerosp. Eng.* 25 (2), 308–319.
- Fish, J., Wagiman, A., 1993. Multiscale finite element method for a locally nonperiodic heterogeneous medium. *Comput. Mech.* 12 (3), 164–180.
- Gojny, F.H., Wichmann, M., Köpke, U., Fiedler, B., Schulte, K., 2004. Carbon nanotube-reinforced epoxy-composites: enhanced stiffness and fracture toughness at low nanotube content. *Compos. Sci. Technol.* 64 (15), 2363–2371.
- Gojny, F.H., Wichmann, M.H., Fiedler, B., Schulte, K., 2005. Influence of different carbon nanotubes on the mechanical properties of epoxy matrix composites—a comparative study. *Compos. Sci. Technol.* 65 (15), 2300–2313.
- Green, R., 1972. A plasticity theory for porous solids. *Int. J. Mech. Sci.* 14 (4), 215–224.
- Hibbit, Karlsson, Sorensen, 2007. ABAQUS/Standard Analysis User's Manual. Hibbit, Karlsson, Sorensen Inc., USA.
- Lemaitre, J., 1985. A continuous damage mechanics model for ductile fracture. *J. Eng. Mater. Technol.* 107 (1), 83–89.
- Lemaitre, J., 2012. A Course on Damage Mechanics. Springer Science & Business Media.
- Li, J., Ma, P.C., Chow, W.S., To, C.K., Tang, B.Z., Kim, J.-K., 2007. Correlations between percolation threshold, dispersion state, and aspect ratio of carbon nanotubes. *Adv. Funct. Mater.* 17 (16), 3207–3215.
- Namilae, S., Chandra, N., 2005. Multiscale model to study the effect of interfaces in carbon nanotube-based composites. *J. Eng. Mater. Technol.* 127 (2), 222–232.
- Perić, D., 1993. On a class of constitutive equations in viscoplasticity: formulation and computational issues. *Int. J. Numer. Methods Eng.* 36 (8), 1365–1393.
- Qiu, J., Zhang, C., Wang, B., Liang, R., 2007. Carbon nanotube integrated multifunctional multiscale composites. *Nanotechnology* 18 (27).
- Rahmat, M., Hubert, P., 2011. Carbon nanotube–polymer interactions in nanocomposites: a review. *Compos. Sci. Technol.* 72 (1), 72–84.
- Rai, A., Subramanian, N., Chattopadhyay, A., 2016. Investigation of piezo-resistivity in CNT nano-composites under damage. *SPIE Smart Structures and Materials+ Nondestructive Evaluation and Health Monitoring*, International Society for Optics and Photonics.
- Rai, A., Subramanian, N., Koo, B., Chattopadhyay, A., 2016. Multiscale damage analysis of cnt nanocomposite using a continuum damage mechanics approach. *J. Compos. Mater.* doi:10.1177/0021998316654304.
- Ren, Y., Fu, Y., Liao, K., Li, F., Cheng, H., 2004. Fatigue failure mechanisms of single-walled carbon nanotube ropes embedded in epoxy. *Appl. Phys. Lett.* 84 (15), 2811–2813.
- Romanov, V., Lomov, S.V., Gorbatiikh, L., Verpoest, I., 2013. A novel approach to modelling of fiber-reinforced composites with carbon nanotubes. In: *Proceedings of the International Conference on Composite Materials* 19.
- Romanov, V.S., Lomov, S.V., Verpoest, I., Gorbatiikh, L., 2015. Modelling evidence of stress concentration mitigation at the micro-scale in polymer composites by the addition of carbon nanotubes. *Carbon* 82, 184–194.
- Seidel, G.D., Lagoudas, D.C., 2006. Micromechanical analysis of the effective elastic properties of carbon nanotube reinforced composites. *Mech. Mater.* 38 (8), 884–907.
- Simo, J.C., Hughes, T.J., 2006. *Computational Inelasticity*, 7. Springer Science & Business Media.
- Sochi, E.J., 2012. Challenges for insertion of structural nanomaterials in aerospace applications. In: *15th European Conference on Composite Materials*.
- Subramanian, N., Koo, B., Rai, A., Chattopadhyay, A., 2015. A multiscale damage initiation model for CNT-enhanced epoxy polymers. In: *20th International Conference on Composite Materials*. Copenhagen, Denmark. 4410–8.
- Subramanian, N., Rai, A., Chattopadhyay, A., 2015. Atomistically informed stochastic multiscale model to predict the behavior of carbon nanotube-enhanced nanocomposites. *Carbon* 94, 661–672.
- Thostenson, E.T., Ren, Z., Chou, T.-W., 2001. Advances in the science and technology of carbon nanotubes and their composites: a review. *Compos. Sci. Technol.* 61 (13), 1899–1912.
- Valavala, P., Odegard, G., 2005. Modeling techniques for determination of mechanical properties of polymer nanocomposites. *Rev. Adv. Mater. Sci.* 9, 34–44.
- Wicks, S.S., de Villoria, R.G., Wardle, B.L., 2010. Interlaminar and intralaminar reinforcement of composite laminates with aligned carbon nanotubes. *Compos. Sci. Technol.* 70 (1), 20–28.
- Yang, S., Cho, M., 2008. Scale bridging method to characterize mechanical properties of nanoparticle/polymer nanocomposites. *Appl. Phys. Lett.* 93 (4).
- Yang, S., Yu, S., Ryu, J., Cho, J.-M., Kyoung, W., Han, D.-S., Cho, M., 2013. Non-linear multiscale modeling approach to characterize elastoplastic behavior of CNT/polymer nanocomposites considering the interphase and interfacial imperfection. *Int. J. Plast.* 41, 124–146.
- Yu, X., Kwon, E., 2009. A carbon nanotube/cement composite with piezoresistive properties. *Smart Mater. Struct.* 18 (5), 055010.
- Zhang, J., Koo, B., Subramanian, N., Liu, Y., Chattopadhyay, A., 2016. An optimized cross-linked network model to simulate the linear elastic material response of a smart polymer. *J. Intell. Mater. Syst. Struct.* 27 (11), 1461–1475.
- Zhou, Y., Pervin, F., Lewis, L., Jeelani, S., 2007. Experimental study on the thermal and mechanical properties of multi-walled carbon nanotube-reinforced epoxy. *Mater. Sci. Eng.: A* 452, 657–664.
- Zhou, Y., Pervin, F., Lewis, L., Jeelani, S., 2008. Fabrication and characterization of carbon/epoxy composites mixed with multi-walled carbon nanotubes. *Mater. Sci. Eng.: A* 475 (1), 157–165.